



**HAL**  
open science

## High-precision strontium isotope analysis of geological samples by thermal ionisation mass spectrometry

Tom Henshall, David L Cook, Marion Gar on, Maria Schönbächler

### ► To cite this version:

Tom Henshall, David L Cook, Marion Gar on, Maria Schönbächler. High-precision strontium isotope analysis of geological samples by thermal ionisation mass spectrometry. *Chemical Geology*, 2018, 482, pp.113-120. 10.1016/j.chemgeo.2018.02.010 . hal-03708720

**HAL Id: hal-03708720**

**<https://hal.science/hal-03708720>**

Submitted on 29 Jun 2022

**HAL** is a multi-disciplinary open access archive for the deposit and dissemination of scientific research documents, whether they are published or not. The documents may come from teaching and research institutions in France or abroad, or from public or private research centers.

L'archive ouverte pluridisciplinaire **HAL**, est destinée au dépôt et à la diffusion de documents scientifiques de niveau recherche, publiés ou non, émanant des établissements d'enseignement et de recherche français ou étrangers, des laboratoires publics ou privés.

1 **High-precision Strontium Isotope Analysis of Geological Samples by Thermal**  
2 **Ionisation Mass Spectroscopy**

3  
4 Tom Henshall<sup>a</sup>, David L. Cook<sup>a\*</sup>, Marion Garçon<sup>a</sup>, Maria Schönbacher<sup>a</sup>

5  
6 <sup>a</sup> Institut für Geochemie und Petrologie, ETH Zürich, Clausiusstrasse 25, 8092 Zürich,  
7 Switzerland.

8  
9 \*To whom correspondence should be addressed. Email: [david.cook@erdw.ethz.ch](mailto:david.cook@erdw.ethz.ch)

10  
11 Accepted in Chemical Geology

32 Abstract

33 We present a method for the efficient separation of Sr from geological materials followed  
34 by high-precision measurement of Sr isotopes by thermal ionisation mass spectrometry  
35 (TIMS). These analyses focus on high-precision measurements of the low abundance  
36 isotope  $^{84}\text{Sr}$  (0.56%), which is of high interest for cosmochemical applications. The robust  
37 dataset obtained through the analysis of a range of basalts and anorthosites sheds light  
38 on a number of issues regarding Sr isotopic analyses. Specifically, concerns that analytical  
39 artefacts may produce a spurious signal on  $^{84}\text{Sr}$  have been investigated. The external  
40 reproducibility, based on replicate measurements of the basalt standard BCR-2, for  $\epsilon^{84}\text{Sr}$   
41 is  $\pm 0.36$  (2SD), and is  $\pm 0.51$  (2SD) for repeated analyses of NIST SRM-987. In contrast  
42 with the static measurements of previous work (Moynier et al., 2012; Paton et al., 2013;  
43 Brennecka et al., 2013), our dynamic data reveal no  $^{84}\text{Sr}$  variations in terrestrial rocks or  
44 standard material. The dataset indicates that, by the analytical procedure employed,  $^{84}\text{Sr}$   
45 variations in extra-terrestrial material larger than  $\sim 0.5\epsilon$  are resolvable.

46

47

48

49

50

51

52

53

54

55

56

57

58

59 Keywords: TIMS, strontium isotopes, dynamic measurements

## 60 **1. Introduction**

61 Strontium has four stable isotopes:  $^{84}\text{Sr}$ ,  $^{86}\text{Sr}$ ,  $^{87}\text{Sr}$ , and  $^{88}\text{Sr}$ . The isotope  $^{87}\text{Sr}$  varies due to  
62 ingrowth from the decay of  $^{87}\text{Rb}$  ( $t_{1/2}=48$  Ga) and provides an important chronometer for  
63 geological processes that fractionate Rb from Sr (Goldschmidt, 1937; Hahn and Walling,  
64 1938; Hahn et al., 1943; Papanastassiou and Wasserburg, 1969; McCulloch, 1994; Hans  
65 et al., 2013a; Villa et al., 2015). As well as chronological applications, Sr isotopic data are  
66 versatile tracers for geological and archaeological provenance studies, such as  
67 investigating historical continental weathering and ocean circulation (e.g., Frank, 2000)  
68 and forensic tracing of human and animal migration (e.g., Beard and Johnson, 2000). For  
69 these reasons, Sr isotopes are widely applied in the fields of cosmochemistry, mantle  
70 geochemistry, palaeoceanography, and archaeology. In particular, the  $^{87}\text{Rb}$ - $^{87}\text{Sr}$   
71 chronometer has proved to be a key tool in dating the volatile element depletion of rocky  
72 planets and asteroids (e.g., Papanastassiou and Wasserburg, 1969; McCulloch, 1994).

73 Rubidium, a moderately volatile element, is more volatile than Sr (50 % condensation  
74 temperatures: Rb=800 K, Sr=1464 K (Lodders, 2003)), which led to the preferential loss  
75 of Rb over Sr during condensation and evaporation processes in the nascent solar system  
76 and subsequent fractionation of Rb/Sr ratios. In materials that were highly depleted in  
77 volatiles, extensive Rb loss led to minimal  $^{87}\text{Sr}$  ingrowth. Accordingly, the timing of  
78 fractionation can be gauged by (i) directly measuring the  $^{87}\text{Sr}/^{86}\text{Sr}$  ratio for samples  
79 devoid of Rb, which yields the initial  $^{87}\text{Sr}/^{86}\text{Sr}$  ratio at the time the sample formed or (ii)  
80 measuring the  $^{87}\text{Rb}/^{86}\text{Sr}$  and  $^{87}\text{Sr}/^{86}\text{Sr}$  ratios in the material of interest to determine the  
81 initial  $^{87}\text{Sr}/^{86}\text{Sr}$  ratio using the isochron approach. The slope of a  $^{87}\text{Rb}$ - $^{87}\text{Sr}$  isochron  
82 provides the time information, while the y-axis intercept provides the initial  $^{87}\text{Sr}/^{86}\text{Sr}$   
83 ratio of the reservoir from which the sample originated. This initial  $^{87}\text{Sr}/^{86}\text{Sr}$  ratio is  
84 important because it provides the root ratio for model age calculations.

85 Calcium-aluminium-rich inclusions (CAIs) in primitive meteorites are the oldest material  
86 identified in the solar system (e.g., Bouvier and Wadhwa, 2010). They have highly  
87 refractory compositions and incorporated little Rb during their formation, which led to  
88 minimal  $^{87}\text{Sr}$  ingrowth. Consequently, CAIs provide an estimate for the initial Sr isotopic  
89 composition of the solar system (e.g., Gray et al., 1973; Hans et al., 2013a). The initial

90  $^{87}\text{Sr}/^{86}\text{Sr}$  ratio of CAIs represent a baseline for  $^{87}\text{Sr}$  evolution and calculations of model  
91 ages for volatile depletion in the inner solar system. Calcium-aluminium-rich inclusions,  
92 however, exhibit nucleosynthetic Sr isotopic variations that have been attributed to  
93 excesses in the p-process isotope  $^{84}\text{Sr}$  (Moynier et al., 2012; Paton et al., 2013; Brennecka  
94 et al., 2013). This nucleosynthetic variation is significant for the interpretation of  
95  $^{87}\text{Sr}/^{86}\text{Sr}$  ratios. Due to analytical issues concerning the correction of instrumental mass  
96 bias, it is not possible to accurately identify the anomalous Sr isotope using Sr isotopic  
97 data and traditional approaches alone. Because  $^{87}\text{Sr}$  contains an unknown radiogenic  
98 component from  $^{87}\text{Rb}$  decay, it cannot be used to correct for mass-bias effects. Therefore,  
99  $^{86}\text{Sr}$  and  $^{88}\text{Sr}$  are used for mass-bias correction. Because of this,  $^{84}\text{Sr}$  variations could in  
100 fact be due to variation in  $^{88}\text{Sr}$  or  $^{86}\text{Sr}$  propagating through the mass-bias correction and  
101 cause an apparent effect on  $^{84}\text{Sr}$  (equation 1). Identifying the exact location of the  
102 variation ( $^{84}\text{Sr}$  or  $^{88}\text{Sr}$ ) is of tangible importance, as it may significantly alter our picture  
103 of early solar system volatile element evolution during planet formation. Nucleosynthetic  
104  $^{88}\text{Sr}$  excesses require an upward correction to measured  $^{87}\text{Sr}/^{86}\text{Sr}$  ratios in CAIs (e.g.,  
105 Hans et al., 2013a) and, consequentially, an earlier age for volatile depletion (*i.e.*, Rb loss)  
106 by several Ma. These factors highlight the importance of a well-tested, reproducible  
107 method to measure Sr isotopes at high accuracy and precision.

108 In previous studies, Sr isotopic analyses of terrestrial rocks by thermal ionisation mass  
109 spectrometry (TIMS) yielded different results for dynamic and static acquisition modes.  
110 Despite the fact that all studies were performed on Thermo Scientific Triton TIMS  
111 instruments, static measurements of BCR-2 and BHVO-2 displayed a consistent negative  
112 offset in  $\epsilon^{84}\text{Sr}$ , relative to the NIST SRM 987 Sr standard (Moynier et al., 2012; Paton et  
113 al., 2013; Brennecka et al., 2013), whereas dynamic analyses did not display an offset  
114 (Hans et al., 2013a; Yobregat et al., 2017). Here, we address this discrepancy with far-  
115 reaching implications for cosmochemistry. We collected an extensive dataset for selected  
116 terrestrial samples using both dynamic and static methods. Our samples included a range  
117 of terrestrial rocks (BCR-2, BHVO-2, AGV-2, AN-G, and several anorthosites) to test our  
118 methods for high-precision Sr isotopic measurements for a variety of matrix  
119 compositions. We evaluated pre-existing analytical procedures (Hans et al., 2013a) and  
120 adapted the method to improve the low yields for anorthitic sample matrices. We  
121 reproduced the consistent offset from the NIST SRM 987 Sr standard for static analyses  
122 and demonstrate that the offset is not observed when using a dynamic routine. We also

123 show that instrumental mass-dependent fractionation does not cause the observed offset  
124 between static and dynamic values.

125

## 126 **2. Sample Preparation**

### 127 *2.1. Reagents and materials*

128 Hydrochloric and nitric acids were purified twice in Teflon stills, hydrofluoric acid once.  
129 Boric acid was prepared by the addition of 99.995% pure Puratronic boric crystals  
130 ( $\text{BH}_3\text{O}_3$ ) to 3.5M  $\text{HNO}_3$  to achieve a molarity of 0.45. Reagent grade  $\text{H}_2\text{O}_2$  and Milli-Q grade  
131 (18.2  $\Omega$ ) water (MQ) were used throughout this study.

### 132 *2.2. Selected samples and sample digestion*

133 The NIST SRM 987 Sr standard, four rock standards (the basalts BCR-2 and BHVO-2, the  
134 andesite AGV-2, and the anorthosite AN-G), two anorthite separates (AN-1 and AN-2)  
135 from anorthosites (from Sierra Nevada (California) and Adamello (Italy), respectively),  
136 and one additional whole rock anorthosite (JL-27; from Rum, Scotland) were measured  
137 in this study. The whole rock samples were crushed either with a hydraulic press or  
138 sizeable hammer and powdered with an agate pestle and mortar. For AN-1 and AN-2,  
139 anorthite separates were obtained by crushing, followed by magnetic separation and  
140 hand picking under an optical microscope. The anorthosite rock standard AN-G was  
141 chosen as a proxy for calcium-aluminium-rich inclusions because of their similar, Ca-rich  
142 sample matrices.

143 For each sample, 30 mg of powder were digested in 15 ml Savillex® vials at 100°C  
144 overnight using a mixture of 0.3 ml HF and 0.1 ml  $\text{HNO}_3$ . The sample mass was limited to  
145 30 mg to prevent overloading the column. The samples were dried at 120°C and re-  
146 dissolved in 1 ml of concentrated  $\text{HNO}_3$  and dried. This  $\text{HNO}_3$  dry down was repeated and  
147 was followed by fluxing in 1 ml concentrated HCl overnight. Finally, the samples were  
148 dried and redissolved in 2.5 M HCl. If necessary, samples were placed in an ultra-sonic  
149 bath before loading onto the ion exchange column.

## 150 **3. Ion Exchange Column Chemistry**

151 A two-stage procedure for the separation of Sr from the sample matrix was used and  
152 follows the procedure of Hans et al. (2013a) (Table 1). A Teflon column (resin reservoir  
153 dimensions: 18 cm length, 5 mm inner diameter) was loaded with 3.7 ml of BioRad®  
154 cation resin AG50W-X8 (200-400 mesh). The resin was cleaned and preconditioned with  
155 10 ml MQ followed by 20 ml 2.5M HCl. The sample was loaded in 1 ml 2.5M HCl and matrix  
156 elements were eluted with 17 ml 2.5M HCl before eluting Sr in 9 ml 2.5M HCl. The resin  
157 was then cleaned with 20 ml 6M HCl and reused up to 4 times. The sample elution was  
158 dried at 70°C overnight and then redissolved in 0.5 ml of concentrated HNO<sub>3</sub>. This was  
159 dried to a very small drop and 1 ml of 3M HNO<sub>3</sub> was added for loading onto the second  
160 column.

161 In order to further purify Sr, the Sr elution from the first column was passed through a Sr  
162 spec resin in a Teflon shrink-wrap column (resin reservoir dimensions: 25 mm length, 3  
163 mm inner diameter). The column was filled with 0.2 ml resin, which was cleaned and  
164 preconditioned with 4 ml MQ, 4 ml 0.05M HNO<sub>3</sub> and 4 ml 3M HNO<sub>3</sub>. After the sample was  
165 loaded, matrix elements were eluted with 4 ml 3M HNO<sub>3</sub>. Strontium was eluted in 3 ml  
166 0.05M HNO<sub>3</sub>. The resin was not reused. The Sr fraction was dried at 120°C, re-dissolved  
167 in 1 ml concentrated HNO<sub>3</sub>, and fluxed at 100°C for one hour. The sample was left to cool  
168 and a few drops of H<sub>2</sub>O<sub>2</sub> were added to destroy organics. Subsequently, the sample was  
169 dried at 80°C. A few drops of 6M HCl were added and dried down again. Yields were >90%  
170 and blanks were typically a few hundred picograms. The amount of Sr in the samples  
171 ranged from 2 - 11 µg and, therefore, no blank correction was necessary. A total of nine  
172 full procedural blanks were measured over the course of three years.

### 173 *3.1. AN-G and boric acid*

174 For the AN-G rock standard, an additional step was added to the dissolution procedure.  
175 This included boric acid to prevent the formation of fluorides (Greenwood and Earnshaw,  
176 1997; Yokoyama et al., 1999) and keep Sr in solution, following the procedure outlined  
177 by Connelly et al. (2006). After sample digestion, the samples were dried and then fluxed  
178 in concentrated HNO<sub>3</sub> for 24 hours, after which a mixture of 1 ml 0.45 M boric acid in 3.5  
179 M HNO<sub>3</sub> and 1 ml concentrated HCl was added and fluxed for 24 hours. Samples were  
180 dried and fluxed in 6 M HCl for 24 hours. Samples were then dried and re-dissolved in 1  
181 ml 2.5 M HCl for loading on the cation column. Because boric acid may affect the  
182 behaviour of elements on the resin, and therefore the Sr elution curve, a column

183 calibration was carried out. This resulted in the Sr elution being extended to a total of 14  
184 ml, now including 5 ml of the matrix elution (Table 1).

## 185 **4. Mass Spectrometry**

### 186 *4.1. Filament loading and measurement procedure*

187 All measurements were performed on a Triton Multicollector Thermal Ionisation Mass  
188 Spectrometer (TIMS) at ETH Zürich. The purified Sr was taken up in 10 – 20  $\mu\text{L}$  of 6M HCl  
189 and left to dissolve for an hour. This volume was varied to achieve 1  $\mu\text{L}$  loads that  
190 contained  $\sim 500\text{ng}$  Sr, depending on the Sr content of the sample. One  $\mu\text{L}$  of the dissolved  
191 sample was combined with 1  $\mu\text{L}$  Ta phosphate activator solution and mixed using a  
192 syringe and capillary tubing. The 2  $\mu\text{L}$  solution was then loaded onto the center of a Re  
193 filament, which was then glowed to a dull-red for a few seconds until the deposit turned  
194 white. Prior to loading, filaments were outgassed at 4 A for two hours and 4.5 A for thirty  
195 minutes. All filament loads contained roughly the same amount of Sr, whether the sample  
196 material is BCR-2, NIST 987 or other. Processing 30 mg of BCR-2 results in sufficient Sr  
197 ( $\sim 10.4 \mu\text{g}$ ) for 20 filament loads.

198 The filaments were heated to 3500 mA ( $\sim 1,500^\circ\text{C}$ ) over two hours. Autofocusing and  
199 zoom optics were used to obtain flat and well-centred peaks. Masses from 84 – 88 amu  
200 were measured with 20V on the  $^{88}\text{Sr}$  signal. The electronic baseline was measured for 30s  
201 prior to each block of measurements and subtracted from all signal intensities. Amplifier  
202 rotation was used after every block (20 integrations) to average differences in relative  
203 amplifier gains. A two-line acquisition scheme (dynamic protocol) was employed in order  
204 to cancel out variations in Faraday cup efficiencies. One integration lasted 8.4 seconds. In  
205 order for the signal to decay to background levels between lines, delays of 4 seconds and  
206 8 seconds were used after lines 1 and 2, respectively. These delays are sufficient that the  
207 signal decays to a level in the Faraday cups at which it does not affect the measurement  
208 of isotopes on the following line (Hans et al., 2013b). One two-line integration lasted  $\sim 30$   
209 seconds and one total sample measurement lasted up to 5 and a half hours. Generally, 15-  
210 30 blocks of 20 integrations were obtained during this time and a 2 sigma outlier  
211 rejection was applied. Levels of  $^{85}\text{Rb}$ , monitored for interference correction, were  
212 negligible due to the efficient chemical separation procedure and the fact that remaining  
213 Rb in the filament load evaporates at a lower temperature than that at which Sr isotopes  
214 are measured. Sample measurements were interspersed with NIST SRM 987 Sr standard

215 analyses. Sr intensities of standards and samples were corrected for gain, baseline and  
 216 interferences online. The calculation of static and dynamic ratios was performed offline  
 217 after measurement following equations (Eq.1 and Eq.2) detailed below. The data are  
 218 presented as  $\epsilon^{84}\text{Sr}$ , which is defined as the deviation from the average  $^{84}\text{Sr}/^{86}\text{Sr}$  ratio of  
 219 the NIST SRM 987 standard of each analytical session expressed in parts per ten thousand  
 220 ( $\epsilon^{84}\text{Sr} = [({}^{84}\text{Sr}/{}^{86}\text{Sr})_{\text{sample}}/({}^{84}\text{Sr}/{}^{86}\text{Sr})_{\text{standard}} - 1] \times 10^4$ ).

221

#### 222 4.2. Calculation of static ratios

223 Two different measurement routines (static and dynamic) were investigated as they have  
 224 been shown to produce dissimilar results (Hans et al., 2013a,b; Yobregat et al., 2017). For  
 225 static measurements, the signal intensity of  $^{84,86,88}\text{Sr}$  (and  $^{85}\text{Rb}$ ) were analysed  
 226 simultaneously and instrumental mass bias was corrected using the exponential law and  
 227  $\left(\frac{{}^{88}\text{Sr}}{{}^{86}\text{Sr}}\right)_{\text{True}} = 8.3752$  (Thirlwall, 1991). Given the cup configuration (Table 2), the static  
 228 ratio,  $\left(\frac{{}^{84}\text{Sr}}{{}^{86}\text{Sr}}\right)_{\text{Static 1}}$ , from acquisition line 1 can be written as:

$$229 \left(\frac{{}^{84}\text{Sr}}{{}^{86}\text{Sr}}\right)_{\text{Static 1}} = \left(\frac{{}^{84}\text{Sr}}{{}^{86}\text{Sr}}\right)_{\text{Meas 1}} \times \left(\frac{m_{84}}{m_{86}}\right)^f \quad \text{with } f = \frac{\ln\left(\frac{\left(\frac{{}^{88}\text{Sr}}{{}^{86}\text{Sr}}\right)_{\text{True}}}{\left(\frac{{}^{88}\text{Sr}}{{}^{86}\text{Sr}}\right)_{\text{Meas 1}}}\right)}{\ln\left(\frac{m_{88}}{m_{86}}\right)} \quad (\text{Eq. 1})$$

230

231 Where  $m_{84}$ ,  $m_{86}$ , and  $m_{88}$  are the atomic masses of isotopes  $^{84}\text{Sr}$ ,  $^{86}\text{Sr}$ , and  $^{88}\text{Sr}$ ,  
 232 respectively.  $\left(\frac{{}^{84}\text{Sr}}{{}^{86}\text{Sr}}\right)_{\text{Meas 1}}$  and  $\left(\frac{{}^{88}\text{Sr}}{{}^{86}\text{Sr}}\right)_{\text{Meas 1}}$  are the ratios measured on acquisition line 1.

233 Since the measured Sr ion-beam intensities are function of faraday collector efficiencies  
 234 and amplifier gains, we can write:

$$235 \left(\frac{{}^{84}\text{Sr}}{{}^{86}\text{Sr}}\right)_{\text{Meas 1}} = \frac{I^{84}\text{Sr}_{\text{Meas 1}}}{I^{86}\text{Sr}_{\text{Meas 1}}} = \frac{I^{84}\text{Sr}_1 \times C_{L1} \times G_{L1}}{I^{86}\text{Sr}_1 \times C_{H1} \times G_{H1}}$$

$$236 \text{ and } \left(\frac{{}^{88}\text{Sr}}{{}^{86}\text{Sr}}\right)_{\text{Meas 1}} = \frac{I^{88}\text{Sr}_{\text{Meas 1}}}{I^{86}\text{Sr}_{\text{Meas 1}}} = \frac{I^{88}\text{Sr}_1 \times C_{H3} \times G_{H3}}{I^{86}\text{Sr}_1 \times C_{H1} \times G_{H1}}$$

237 where  $I^{84}\text{Sr}_1$ ,  $I^{86}\text{Sr}_1$ , and  $I^{88}\text{Sr}_1$  are the “ true ” intensities of the different Sr isotope  
 238 beams on acquisition lines 1;  $C_{L1}$ ,  $C_{H1}$ , and  $C_{H3}$  are the efficiencies of the faraday collectors  
 239 L1, H1, and H3 that change with time depending on instrument use;  $G_{L1}$ ,  $G_{H1}$ , and  $G_{H3}$  are

240 the gains of the amplifiers to which the faraday collectors L1, H1, and H3 are attached.

241 Using this notation, (Eq.1) can be re-written as follows:

$$242 \left( \frac{^{84}\text{Sr}}{^{86}\text{Sr}} \right)_{\text{Static 1}} = \frac{I^{84}\text{Sr}_1 \times C_{L1} \times G_{L1}}{I^{86}\text{Sr}_1 \times C_{H1} \times G_{H1}} \times \exp \left( \frac{\ln \left( \frac{\left( \frac{^{88}\text{Sr}}{^{86}\text{Sr}} \right)_{\text{True}}}{\frac{I^{88}\text{Sr}_1 \times C_{H3} \times G_{H3}}{I^{86}\text{Sr}_1 \times C_{H1} \times G_{H1}}} \right)}{\ln \left( \frac{m_{88}}{m_{86}} \right)} \times \ln \left( \frac{m_{84}}{m_{86}} \right) \right)$$

$$243 \Leftrightarrow \left( \frac{^{84}\text{Sr}}{^{86}\text{Sr}} \right)_{\text{Static 1}} = \frac{I^{84}\text{Sr}_1 \times C_{L1} \times G_{L1}}{I^{86}\text{Sr}_1 \times C_{H1} \times G_{H1}} \times \left( \frac{\left( \frac{^{88}\text{Sr}}{^{86}\text{Sr}} \right)_{\text{True}}}{\frac{I^{88}\text{Sr}_1 \times C_{H3} \times G_{H3}}{I^{86}\text{Sr}_1 \times C_{H1} \times G_{H1}}} \right)^\varphi \text{ with } \varphi = \frac{\ln \left( \frac{m_{84}}{m_{86}} \right)}{\ln \left( \frac{m_{88}}{m_{86}} \right)}$$

$$244 \Leftrightarrow \left( \frac{^{84}\text{Sr}}{^{86}\text{Sr}} \right)_{\text{Static 1}} = \frac{I^{84}\text{Sr}_1}{I^{86}\text{Sr}_1} \times \left( \frac{^{88}\text{Sr}}{^{86}\text{Sr}} \right)_{\text{True}}^\varphi \times \left( \frac{I^{88}\text{Sr}_1}{I^{86}\text{Sr}_1} \right)^{-\varphi} \times \left( \frac{C_{L1} \times G_{L1}}{C_{H1} \times G_{H1}} \right) \times \left( \frac{C_{H3} \times G_{H3}}{C_{H1} \times G_{H1}} \right)^{-\varphi}$$

245 Using  $m_{84} = 83.91319$ ;  $m_{86} = 85.90926$  and  $m_{88} = 87.905612$  (Wang et al., 2012),  $\varphi$  is

246 equal to  $-1.02337$ , hence the static ratio scales to  $\sim \frac{C_{L1} \times G_{L1} \times C_{H3} \times G_{H3}}{(C_{H1} \times G_{H1})^2}$ . Assuming that the

247 amplifier gains are properly calibrated and do not vary during a run (i.e.  $G_{H1} = G_{L1} = G_{H3} =$

248 1), a simple sensitivity test shows that if faraday collector L1 deteriorates faster than

249 faraday collectors H1 and H3 so that  $\frac{C_{L1}}{C_{H1}} = 0.999900$  and  $\frac{C_{H3}}{C_{H1}} = 1$ , then the static  $\left( \frac{^{84}\text{Sr}}{^{86}\text{Sr}} \right)$  ratio

250 will be shifted by  $-100$  ppm (see Garçon et al., 2018 for more details on the calculation).

251 Long-term accuracy and precision of static ratios should thus degrade slowly through

252 time as collector performance deteriorates.

253

### 254 4.3. Calculation of dynamic ratios

255 A two-line dynamic acquisition scheme was also used for the determination of  $^{84}\text{Sr}/^{86}\text{Sr}$

256 ratios. Varying the magnet settings enabled the measurement of Sr isotopes in different

257 faraday cups from line 1 to line 2 (Table 2). Dynamic ratios are calculated assuming that

258 Sr mass fractionation follows an exponential law during the run. The dynamic  $^{84}\text{Sr}/^{86}\text{Sr}$

259 ratio,  $\left( \frac{^{84}\text{Sr}}{^{86}\text{Sr}} \right)_{\text{Dyn 1}}$ , is obtained by combining the  $^{84}\text{Sr}/^{86}\text{Sr}$  ratio measured on line 1,

260  $\left( \frac{^{84}\text{Sr}}{^{86}\text{Sr}} \right)_{\text{Meas 1}}$ , with the  $^{88}\text{Sr}/^{86}\text{Sr}$  ratio measured on line 2,  $\left( \frac{^{88}\text{Sr}}{^{86}\text{Sr}} \right)_{\text{Meas 2}}$ , to minimize the

261 relative difference of efficiencies and amplifier gains between Faraday collectors L1 and  
 262 H1. This gives:

$$\begin{aligned}
 263 \quad \left(\frac{{}^{84}\text{Sr}}{{}^{86}\text{Sr}}\right)_{\text{Dyn 1}} &= \left(\frac{{}^{84}\text{Sr}}{{}^{86}\text{Sr}}\right)_{\text{Meas 1}} \times \left(\frac{m_{84}}{m_{86}}\right)^f \quad \text{with } f = \frac{\ln\left(\frac{\left(\frac{{}^{88}\text{Sr}}{{}^{86}\text{Sr}}\right)_{\text{True}}}{\left(\frac{{}^{88}\text{Sr}}{{}^{86}\text{Sr}}\right)_{\text{Meas 2}}}\right)}{\ln\left(\frac{m_{88}}{m_{86}}\right)} \\
 264 \quad \Leftrightarrow \left(\frac{{}^{84}\text{Sr}}{{}^{86}\text{Sr}}\right)_{\text{Dyn 1}} &= \left(\frac{{}^{84}\text{Sr}}{{}^{86}\text{Sr}}\right)_{\text{Meas 1}} \times \left(\frac{{}^{88}\text{Sr}}{{}^{86}\text{Sr}}\right)_{\text{True}}^{\varphi} \times \left(\frac{{}^{88}\text{Sr}}{{}^{86}\text{Sr}}\right)_{\text{Meas 2}}^{-\varphi} \quad (\text{Eq. 2})
 \end{aligned}$$

265 With ion-beam intensities, this gives:

$$266 \quad \left(\frac{{}^{84}\text{Sr}}{{}^{86}\text{Sr}}\right)_{\text{Dyn 1}} = \frac{I^{84}\text{Sr}_1}{I^{86}\text{Sr}_1} \times \left(\frac{{}^{88}\text{Sr}}{{}^{86}\text{Sr}}\right)_{\text{True}}^{\varphi} \times \left(\frac{I^{88}\text{Sr}_2}{I^{86}\text{Sr}_2}\right)^{-\varphi} \times \left(\frac{C_{L1} \times G_{L1}}{C_{H1} \times G_{H1}}\right)^{1+\varphi}$$

267 Because  $\varphi$  is  $\sim -1$ , faraday cup efficiencies and amplifier gains (*i.e.*,  $\frac{C_{L1} \times G_{L1}}{C_{H1} \times G_{H1}}$ ) almost divide  
 268 out in the dynamic calculation of  $\left(\frac{{}^{84}\text{Sr}}{{}^{86}\text{Sr}}\right)$ , hence dynamic ratios are much less sensitive to  
 269 faraday collector deteriorations and changes in amplifier gains than static ratios. Using  
 270 the same sensitivity test as above for the static ratio, that is assuming that  $G_{H1} = G_{L1} = 1$   
 271 and the faraday collectors degraded such that  $\frac{C_{L1}}{C_{H1}} = 0.999900$ , one can show that the  
 272 dynamic ratio will only be shifted by +2.3 ppm (Garçon et al, 2018). In other words, the  
 273 calculation of dynamic ratios mathematically cancels out  $\sim 97.7\%$  of the component of  
 274 imprecision and inaccuracy arising from collector inefficiencies and amplifier gain drift  
 275 during measurement. This is the reason why the long-term precision and accuracy of  
 276 dynamic ratios is, in general, much better than that of static ratios.

277

## 278 5. Results and Discussion

### 279 5.1. Precision and accuracy of standard measurements

280 The long-term static average of  ${}^{84}\text{Sr}/{}^{86}\text{Sr}$  for the NIST SRM 987 Sr standard is 0.056495  
 281  $\pm 0.000003$ , (2SD; n=52). The data are in good agreement with those reported by other  
 282 groups (Table 3; Andreasen and Sharma, 2007; Moynier et al., 2012; Hans et al., 2013a;  
 283 Brennecke et al., 2013; Yobregat et al., 2017). The slight differences in absolute ratios for  
 284 standards between this study and others do not affect the data comparison between the

285 studies because epsilon values are calculated relative to the standards for each analytical  
286 session. Furthermore, our long-term dynamic average of  $^{84}\text{Sr}/^{86}\text{Sr}$  for the NIST SRM 987  
287 Sr standard is  $0.056497 \pm 0.000003$  is more accurate as it is not dependent on Faraday  
288 cup deterioration. Repeat measurements of the NIST SRM 987 Sr standard that was  
289 processed through ion chromatography define a dynamic value of  $\epsilon^{84}\text{Sr} -0.08 \pm 0.19$  (2SE;  
290  $n= 5$ , Table 4) and is thus zero within uncertainty. This demonstrates that the chemical  
291 separation procedure does not affect the Sr isotopic composition of samples.

## 292 *5.2. Precision and accuracy of sample measurements*

293 For data acquired in dynamic mode, the terrestrial rocks define an average  $\epsilon^{84}\text{Sr}$  value of  
294  $-0.04 \pm 0.09$  (2SE), which is within uncertainty of 0, as defined by the NIST SRM 987 Sr  
295 standard (Table 4; supplementary material Table A1). In contrast, for static acquisition,  
296 the mean of all terrestrial rocks is resolved from 0, an  $\epsilon^{84}\text{Sr}$  value of  $-0.15 \pm 0.09$  (2SE).  
297 These averages are based on 27 separate samples measured over two years. The data  
298 broadly agree with those in the literature within uncertainty and reproduce the negative  
299 offset observed in terrestrial material for  $\epsilon^{84}\text{Sr}$  when measured in static mode (Table 4).  
300 This offset is not observed in dynamic mode (Fig. 1 and 2).

301 For BCR-2 and BHVO-2 in particular, our static measurements also confirm the previously  
302 reported negative offsets in  $\epsilon^{84}\text{Sr}$  (Table 4, Andreasen and Sharma, 2007; Paton et al.,  
303 2013; Brennecka et al., 2013). However, the average  $\epsilon^{84}\text{Sr}$  values for dynamic  
304 measurements of BCR-2 ( $-0.12 \pm 0.11$ ) and BHVO-2 ( $0.04 \pm 0.24$ ) do not display a resolved  
305 negative offset (Fig. 1 and 2). Terrestrial Sr is not expected to show non-mass dependent  
306 variations in  $^{84}\text{Sr}/^{86}\text{Sr}$  ratios. Thus, the absence of  $\epsilon^{84}\text{Sr}$  deficits for dynamic  
307 measurements is consistent with expectations. This indicates that, for  $^{84}\text{Sr}$ , dynamic  
308 measurements are more accurate than static ones, consistent with dynamic data for  $\epsilon^{84}\text{Sr}$   
309 reported by Hans et al. (2013a) and Yobregat et al. (2017). The external reproducibility  
310 (2SD) on  $\epsilon^{84}\text{Sr}$ , based on 10 replicate analyses of BCR-2, is 0.36 and is similar to the long-  
311 term reproducibility of SRM-987 ( $\pm 0.51$ ). The values above demonstrate the high degree  
312 of accuracy and precision of the measurements.

313

## 314 *5.3. Dynamic vs. static data acquisition*

315 Static measurements have the advantage of time efficiency and good internal precision.  
316 However, a static routine fails to account for changes in individual cup efficiencies over  
317 time. Dynamic acquisition mode overcomes this problem (*e.g.*, Hans et al., 2013a; Roth et  
318 al., 2013). The discrepancy between dynamic and static measurements, with dynamic  
319 analyses yielding values closer to zero (Hans et al., 2013a,b; Yobregat et al., 2017) is  
320 reproduced in this study (Fig. 2). For example, the static line 1 results for BCR-2 are  
321 characterised by a negative average  $\epsilon^{84}\text{Sr}$  value of  $-0.20 \pm 0.15$  (2SE), which is within  
322 uncertainty of the range of -0.10 to -0.18 reported by other studies using only a static  
323 routine (Andreasen and Sharma, 2007; Brennecka et al., 2013; Paton et al., 2013). Static  
324 line 2 results also display a negative offset of slightly smaller magnitude than line 1. This  
325 unusual signature in terrestrial material has been attributed to possible contamination  
326 of the NIST SRM Sr standard SRM 987 during production or nuclear field shift effects  
327 (Moynier et al., 2012; Fujii et al., 2009).

328 Dynamic analyses, however, yield  $\epsilon^{84}\text{Sr}$  data that do not show resolved negative shifts,  
329 which indicates that the shift may be of analytical origin. Possible explanations include:  
330 (i) varying faraday cup efficiencies that are cancelled out by the dynamic routine, (ii)  
331 rapid changes in mass fractionation between magnet settings that lead to inaccurate mass  
332 bias correction for the dynamic data, (iii) insufficient settling of the amplifiers between  
333 magnet jumps from one line to the next (signal decay), (iv) matrix effects that lead to  
334 erroneous mass bias correction, (v) interferences, or (vi) ion beam truncation.

335

### 336 *5.3.1. Faraday cup efficiency*

337 Changes in faraday collector efficiencies depend on instrument use and the amount of  
338 ions collected in the cups through their life. Because previous studies reported similar  
339 negative  $\epsilon^{84}\text{Sr}$  values for static data but likely did not use their instrument the same way,  
340 the static-dynamic offset is unlikely to be due to problems with varying cup efficiencies  
341 through time. Moreover, there is no obvious reason for the collector efficiencies to be  
342 different between standards and samples, as required to explain the static-dynamic offset  
343 between terrestrial samples and the NIST SRM Sr standard.

344

### 345 *5.3.2. Rapid changes in instrumental mass bias*

346 Roth et al. (2014) reported that fast rates of isotopic fractionation during dynamic  
347 measurements of Nd isotopic ratios by TIMS can introduce an analytical bias. If the rate  
348 of instrumental mass-dependent isotopic fractionation is fast relative to the time  
349 between measurement lines, the isotopic ratio used for internal normalisation can be  
350 unsuitable. Consequently, Nd isotopic anomalies relative to terrestrial values reported by  
351 Upadhyay et al. (2009) were suggested to be analytical artefacts (Roth et al., 2014). This  
352 effect might also be significant for dynamic measurements of  $^{84}\text{Sr}/^{86}\text{Sr}$  ratios by TIMS.  
353 Fractionation of  $^{88}\text{Sr}/^{86}\text{Sr}$  ratios between lines one and two could cause line two  $^{88}\text{Sr}/^{86}\text{Sr}$   
354 ratios (measured 8 seconds after line 1) to be unsuitable for the mass bias correction of  
355 line one  $^{84}\text{Sr}/^{86}\text{Sr}$  ratios. Given the collector configuration (Table 2), it is expected that  
356 the normal fractionation of Sr through the run (i.e.  $^{88}\text{Sr}/^{86}\text{Sr}$  increase through time) would  
357 bias the dynamic  $^{84}\text{Sr}/^{86}\text{Sr}$  ratio towards higher than true value for high fractionation  
358 rate. In their study, Yobregat et al. (2017) argued that the average fractionation rate of  
359 their runs was too low to account for the observed dynamic-static offset, therefore ruling  
360 out the possibility of significantly shifting the dynamic  $^{84}\text{Sr}/^{86}\text{Sr}$  ratios with this process.  
361 Our runs have, on average, higher fractionation rates than Yobregat et al. (2017), but like  
362 them, we do not believe that the instrumental fractionation of Sr in between acquisition  
363 lines is responsible for the measured static-dynamic offset in  $\epsilon^{84}\text{Sr}$  values. The detailed  
364 analyses of several of our runs revealed no obvious correlation between the mean  
365 fractionation rate of the runs and the resulting dynamic  $^{84}\text{Sr}/^{86}\text{Sr}$  ratios. Moreover, one  
366 of our BCR-2 run displays a reverse fractionation trend (run with a negative mean  
367 fractionation rate), which should theoretically results in a dynamic  $\epsilon^{84}\text{Sr}$  value lower than  
368 the true value. Nevertheless, this particular run still returns a less negative dynamic  $\epsilon^{84}\text{Sr}$   
369 value ( $\epsilon_{\text{dynamic}}^{84}\text{Sr} = -0.13 \pm 0.29$  (2SE)) than the static value from line one ( $\epsilon_{\text{static line 1}}^{84}\text{Sr} = -0.29$   
370  $\pm 0.25$  (2SE)). Therefore, instrumental fractionation of  $^{88}\text{Sr}/^{86}\text{Sr}$  ratios between line 1 and  
371 line 2 likely does not cause the observed offset between static and dynamic  $\epsilon^{84}\text{Sr}$  values.

372

### 373 *5.3.3. Settling time of the amplifiers*

374 This issue has been tested by Hans et al. (2013a,b) on the same Triton multicollector  
375 thermal ionisation mass spectrometer (TIMS) at ETH Zürich that was used for our study.  
376 These authors showed that remnant signal is not an issue because it decays to

377 background levels within the delay times used during the measurement routine (*i.e.* 4 and  
378 8 seconds after lines one and two, respectively).

#### 379 *5.3.4. Matrix effects*

380 The offsets may be caused because the exponential law used for mass bias correction may  
381 not accurately describe Sr isotopic fractionation in detail. Since the offset is observed for  
382 rock samples and not for the processed NIST SRM 987 Sr standard (Fig. 1, Table 4), the  
383 problem may be due to matrix element(s) from the rock samples that were left behind  
384 after ion exchange chemistry. We did not observe significant levels of Ca, Mg, or Al in the  
385 sample solution after the separation of Sr. Thus, the static offset would require an as yet  
386 unrecognised matrix effect and for the dynamic routine to be more robust against such  
387 matrix effects.

#### 388 *5.3.5. Interferences*

389 Matrix elements present in the analysed solution could also introduce isobaric  
390 interferences on Sr isotopes (*e.g.*,  $^{68}\text{Zn}^{16}\text{O}$  on  $^{84}\text{Sr}$ ). This scenario would require that the  
391 same amount of interfering element is always left in the sample solution and that the  
392 dynamic routine fortuitously corrects for this offset. This is rather unlikely because  
393 different studies (Andreasen and Sharma, 2007; Moynier et al., 2012; Hans et al., 2013a;  
394 Brennecka et al., 2013; Yobregat et al., 2017) observed similar negative offsets despite  
395 using different Sr purification protocols. In general, the amount and composition of any  
396 remaining matrix depends on the ion exchange chemistry protocol and would not be  
397 constant across the above studies.

#### 398 *5.3.6. Ion beam truncation*

399 Yobregat et al. (2017) proposed that truncation of the  $^{88}\text{Sr}$  ion beam was responsible for  
400 the difference in  $\epsilon^{84}\text{Sr}$  values measured in static mode versus those measured in dynamic  
401 mode and that these effects depend on the location of the  $^{88}\text{Sr}$  beam relative to the axial  
402 cup (*i.e.*, H3 vs. H1 on lines 1 and 2, respectively); the farther away the  $^{88}\text{Sr}$  beam is from  
403 the axial cup, the more prone it is to truncation. Yobregat et al. (2017) also observed a  
404 constant, and large difference in the mean mass fractionation factors ( $f$ ) between rock  
405 samples and SRM 987 and showed that such a large difference, combined with beam  
406 truncation, could lead to an apparent offset of 25 ppm in  $\epsilon^{84}\text{Sr}$  values. However, this  
407 hypothesis is not able to explain why their static line 2 values show larger  $\epsilon^{84}\text{Sr}$  effects

408 than those from static line 1 because the  $^{88}\text{Sr}$  beam is collected closer to the axial cup on  
409 line 2. Thus, truncation of the  $^{88}\text{Sr}$  beam does not provide an internally consistent  
410 explanation for the difference between static and dynamic results in their dataset.

411 In addition, beam truncation can explain the difference between static and dynamic  
412 results only if the mean mass fractionation factors observed for analyses of rock samples  
413 compared to those for SRM 987 are distinct. Yobregat et al. (2017) observed a significant  
414 difference (*i.e.*, 0.3), whereas we observed a difference of only 0.004. Moreover, t-tests  
415 performed on our data confirm that there is no significant difference between mass  
416 fractionation factors obtained from terrestrial rock analyses compared to those from  
417 SRM 987 for either static line 1 ( $t = 0.21$ ) or static line 2 ( $t = 0.24$ ). Nevertheless, our  
418 analyses show a systematic offset in  $\epsilon^{84}\text{Sr}$  static values for terrestrial samples. Therefore,  
419 we conclude that truncation of the  $^{88}\text{Sr}$  ion beam is an unlikely explanation for the  
420 difference between  $\epsilon^{84}\text{Sr}$  values measured in static mode versus those measured in  
421 dynamic mode observed in our study.

422 In summary, it cannot be excluded that dynamic acquisition may produce erroneous Sr  
423 compositions that cause the analysed samples to overlap with the NIST SRM 987 Sr  
424 isotopic standard by coincidence. However, we consider this scenario unlikely. Our data  
425 confirm that dynamic analyses consistently produce  $\epsilon^{84}\text{Sr}$  values for terrestrial rock and  
426 mineral samples that are indistinguishable within uncertainty from SRM 987, whereas  
427 static analyses show reproducible negative offsets. While the origin of the offsets  
428 observed using a static routine needs further investigation, the consistency of the  
429 dynamic data strongly suggests that the acquisition of high precision  $\epsilon^{84}\text{Sr}$  data requires  
430 a dynamic routine to obtain accurate results.

## 431 **6. Conclusions**

432 An extensive dataset collected over more than two years confirms that our analytical  
433 procedure provides precise and accurate Sr isotopic measurements. Separation of Sr is  
434 achieved by ion exchange chromatography and isotopic compositions are measured by  
435 TIMS. Data for terrestrial rocks acquired in dynamic mode display  $\epsilon^{84}\text{Sr}$  values within  
436 uncertainty of 0. The discrepancy between static and dynamic acquisition schemes  
437 reported by Hans et al. (2013a) and Yobregat et al. (2017) is confirmed, and the dynamic  
438 mode is found to be more accurate. Previously reported deficits for  $\epsilon^{84}\text{Sr}$  in terrestrial

439 material (Andreasen and Sharma, 2007; Moynier et al., 2012; Brennecka et al., 2013;  
440 Paton et al., 2013) were reproduced in this study and are best understood as analytical  
441 artefacts caused by data acquisition in static mode. Looking to the future, Sr isotopic  
442 measurements for a similar range of terrestrial rocks by inductively coupled plasma mass  
443 spectrometry (ICP-MS) would provide a means of testing if the deficit is unique to TIMS  
444 measurements carried out in static mode, which then may provide insight into the origin  
445 of the artefacts.

446

#### 447 **Acknowledgements**

448 This work has been carried out within the frame of the National Centre for Competence  
449 in Research PlanetS supported by the Swiss National Science Foundation. MG received  
450 funds from the Ambizione program of the Swiss National Science Foundation under the  
451 grant N° PZ00P2\_161218. We thank Julien Leuthold for providing anorthosite sample  
452 material and Irene Ivanov-Bucher for her help in sample preparation and mineral  
453 separation. We also thank Colin Maden and Donat Niederer for helping to maintain the  
454 Triton TIMS instrument at ETH Zürich.

455

456

457

458

459

#### 460 **References**

461

462 Andreasen R., Sharma M., Mixing and homogenisation in the early solar system: clues from Sr,  
463 Ba, Nd, and Sm isotopes in meteorites, *Astrophys. J.* 665 (2007) 874-883.

464

465 Beard B.L., Johnson C.M., Strontium isotope composition of skeletal material can  
466 determine the birth place and geographic mobility of humans and animals, *J.*  
467 *Forensic Sci.* 45 (2000) 1049-1061.

468

469 Bouvier A., Wadhwa M., The age of the Solar System redefined by the oldest Pb-Pb age of  
470 a meteoritic inclusion, *Nat. Geosci.* 3 (2010) 637-641.

471

472 Brennecka G. A., Borg L. E., Wadhwa M., Evidence for supernova injection into the solar  
473 nebula and the decoupling of r-process nucleosynthesis, *Proc. Natl. Acad. Sci. U.S.A.* 110  
474 (2013) 17241-17246.  
475  
476 Connelly J.N., Ulfbeck D.G., Thrane K., Bizzarro M., Housh T., A method for purifying Lu and  
477 Hf for analyses by MC-ICP-MS using TODGA resin, *Chem. Geol.* 233 (2006) 126-136.  
478  
479 Frank M., Geochemical proxies of ocean circulation and weathering inputs: radiogenic  
480 isotopes of Nd, Pb, Sr, Hf, and Os. *Earth Environ. Sci.* (2011) 1-7.  
481  
482 Fujii T., Moynier F., Albarede F., The nuclear field shift effect in chemical exchange reactions.  
483 *Chem. Geol.* 267 (2009) 139-156.  
484  
485 Garçon M., Boyet M., Carlson R.W., Horan M. T., Auclair D., Mock T.D., Factors influencing  
486 the precision and accuracy of Nd isotope measurements by thermal ionization  
487 mass spectrometry, *Chemical Geology* (2018), Accepted.  
488  
489 Goldschmidt V.M., The Principles of distribution of chemical elements in mineral and rocks, *J.*  
490 *Chem. Soc.* 0 (1937) 655-673.  
491  
492 Gray C.M., Papanastassiou D.A., Wasserburg G.J., The identification of early condensates  
493 from the solar nebula, *Icarus* 20 (1973) 213-239.  
494  
495 Greenwood N.N., Earnshaw A., *Chemistry of the Elements*, Second Edition (1997) London,  
496 Butterworth 1600 p.  
497  
498 Hahn O., Walling E., Über die möglichkeit geologischer altersbestimmungen  
499 rubidiumhaltiger mineralien un gesteine, *Z. Anorg. Allg. Chem.* 236 (1938) 78-82.  
500  
501 Hahn O., Strassman F., Mattauich J., Ewald H., Geologische altersbestimmungen mit der  
502 strontiummethode, *Chem. Zeitung* 67 (1943) 55-56.  
503  
504 Halliday A.N., Mixing, volatile loss and compositional change during impact-driven  
505 accretion of the Earth, *Nature* 427 (2004) 505-509.  
506  
507 Hans U., Kleine T., Bourdon B., Rb-Sr chronology of volatile depletion in differentiated  
508 protoplanets: BABI, ADOR and ALL revisited, *EPSL* 374 (2013a) 204-214.  
509  
510 Hans U., High-precision strontium isotope measurements on meteorites: implications for the  
511 origin and timing of volatile depletion in the inner solar system, *Doctoral dissertation*  
512 (2013b) ETH Zürich.  
513  
514 Humayun M., Clayton R.N., Potassium isotope cosmochemistry - genetic implications of  
515 volatile element depletion, *Geochim. Cosmochim. Acta* 59 (1995) 2131-2148.  
516  
517 Larimer J.W., Anders E., Chemical fractionations in meteorites-II. Abundance patterns and  
518 their interpretation, *Geochim. Cosmochim. Acta* 56 (1967) 1673-1694.  
519

520 McCulloch M.T., Primitive  $^{87}\text{Sr}/^{86}\text{Sr}$  from an Archaean barite and conjecture on the Earth's age  
521 and origin, *Earth Planet. Sci. Lett.* 126 (1994) 1-13.  
522

523 Moynier F., Day J. M., Okui W., Yokoyama T., Bouvier A., Walker R. J., Podosek F. A,  
524 Planetary-scale strontium isotopic heterogeneity and the age of volatile depletion of  
525 early solar system materials, *Astrophys. J.* 758 (2012) 45-51.  
526

527 Papanastassiou D.A., Wasserburg G.J., Initial strontium isotopic abundances and the  
528 resolution of small time differences in the formation of planetary objects, *Earth Planet.*  
529 *Sci. Lett.* 5 (1969) 361-376.  
530

531 Paton C., Schiller M., Bizzarro, M., Identification of an  $^{84}\text{Sr}$ -depleted carrier in primitive  
532 meteorites and implications for thermal processing in the solar protoplanetary  
533 disk, *Astrophys. J. Lett.* 763 (2013) L40-L45.  
534

535 Roth A.S.G., Neodymium isotopes and evolution of early terrestrial crust, Doctoral dissertation  
536 (2013) ETH Zürich.  
537

538 Roth A.S.G., Scherer E.E., Maden C., Mezger K., Bourdon B., Revisiting the  $^{142}\text{Nd}$  deficits in  
539 the 1.48 Ga Khariar alkaline rocks, India, *Chem. Geol.* 386 (2014) 238-248.  
540

541 Thirlwall M.F., Long-term reproducibility of multicollector Sr and Nd isotope ratio analysis,  
542 *Chem. Geol.* 94 (1991) 85-104.  
543

544 Upadhyay D., Scherer E.E., Mezger K.,  $^{142}\text{Nd}$  evidence for an enriched Hadean reservoir in  
545 cratonic roots, *Nature* 459 (2009) 1118-1121.  
546

547 Villa I.M., De Bièvre P., Holden N.E., Renne P.R., IUPAC-IUGS recommendation of the half-  
548 life of  $^{87}\text{Rb}$ , *Geochim. Cosmochim. Acta* 164 (2015) 382-385.  
549

550 Wang, M., Audi, G., Wapstra, A.H., Kondev, F.G., MacCormick, M., Xu, X., Pfeiffer, B., 2012.  
551 The Ame2012 atomic mass evaluation. *Chinese Phys. C* 36, 1603-2014.  
552 doi:10.1088/1674-1137/36/12/003  
553

554 Yobregat E., Fitoussi C., Bourdon B., A new method for TIMS high precision analysis of Ba and  
555 Sr isotopes for cosmochemical studies, *J. Anal. At. Spectrom.* 32 (2017) 1388-1399.  
556

557 Yokoyama T., Makishima A., Nakamura E., Evaluation of the coprecipitation of incompatible  
558 trace elements with fluoride during silicate rock dissolution by acid digestion, *Chem.*  
559 *Geol.* 157 (1999) 175-187.  
560

561

562

563

564 **Tables and Figures**

**Table 1**

565

Ion chromatography protocol for Sr separation.

Step	Volume (ml)	Solution
<i>Cation column: 3.7 ml BioRad cation resin AGW-X8 (200-400 mesh)</i>		
Cleaning	10	MQ
Preconditioning	20	2.5 M HCl
Load sample	1	2.5 M HCl
Elute matrix	17	2.5 M HCl
Elute Sr	9	2.5 M HCl
Cleaning	20	6 M HCl
<i>Sr spec column: 0.2 ml Sr-spec resin (50-100 <math>\mu</math>m)</i>		
Cleaning	4	MQ
Cleaning	4	0.05 M HNO <sub>3</sub>
Preconditioning	4	3 M HNO <sub>3</sub>
Load sample	1	3 M HNO <sub>3</sub>
Elute matrix	4	3 M HNO <sub>3</sub>
Elute Sr	3	0.05 M HNO <sub>3</sub>

566

567

568

**Table 2**

Faraday Cup configuration for TIMS measurements.

Cup	L3	L2	L1	CC	H1	H2	H3
Line 1	-	-	<sup>84</sup> Sr	<sup>85</sup> Rb	<sup>86</sup> Sr	<sup>87</sup> Sr	<sup>88</sup> Sr
Line 2	<sup>84</sup> Sr	<sup>85</sup> Rb	<sup>86</sup> Sr	<sup>87</sup> Sr	<sup>88</sup> Sr	-	-

The boxes indicate the overlaps exploited for the dynamic analyses. The <sup>88</sup>Sr/<sup>86</sup>Sr ratio from line 2 is used for the mass bias correction of the <sup>84</sup>Sr/<sup>86</sup>Sr ratio from line 1.

**Table 3**

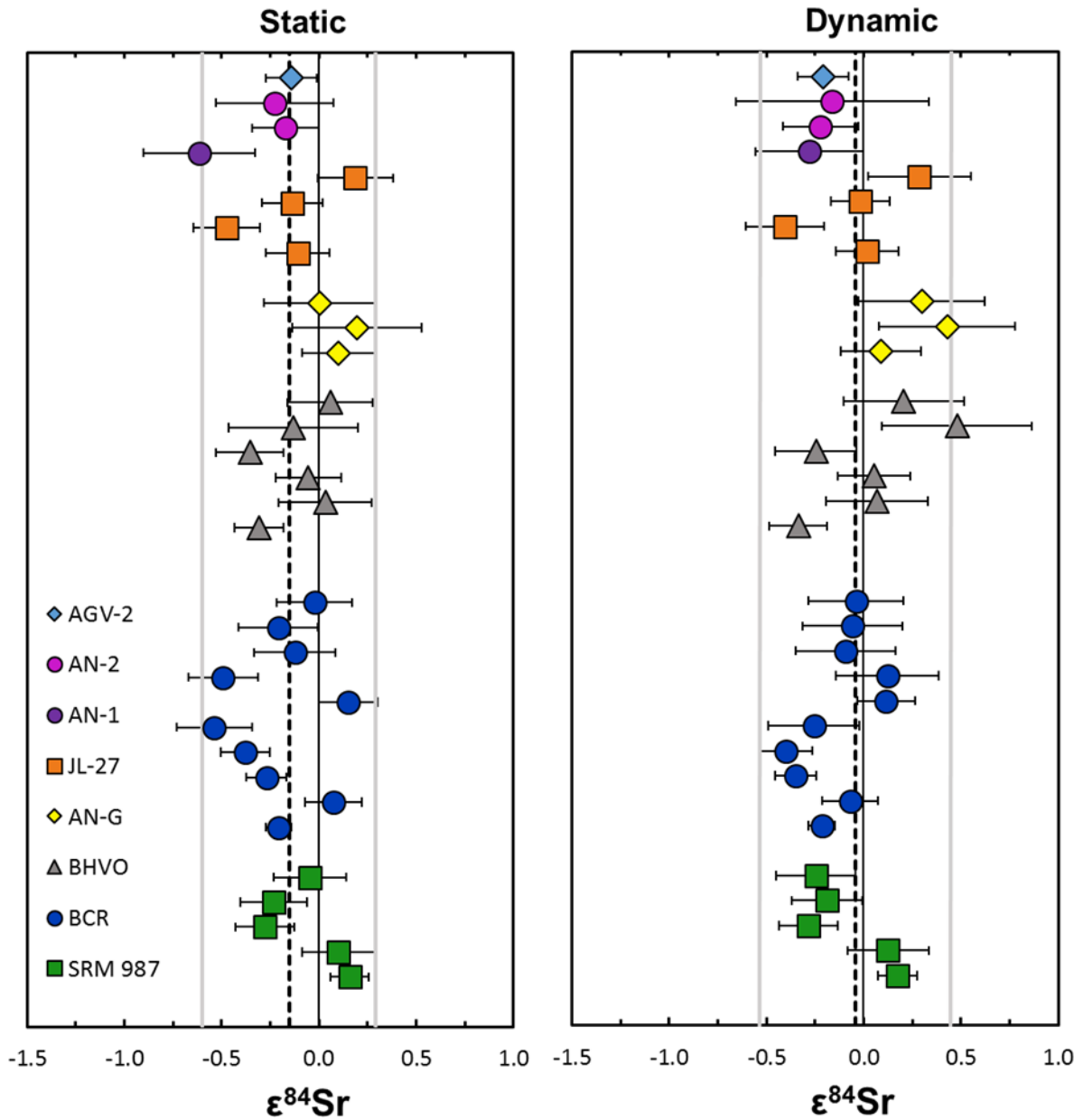
The Sr isotopic composition for NIST SRM-987.

	$^{84}\text{Sr}/^{86}\text{Sr}$	2SD	Mode	n
This study*	0.056497	0.000003	Dynamic	<del>574</del> 52
Hans et al. (2013a)*	0.056495	0.000003	Dynamic	<del>30</del> 30
Yobregat et al. (2017)	0.056492	0.000001	Dynamic	<del>575</del> 35
Brennecke et al. (2013)	0.056493	0.000003	Static	<del>576</del> 15
Moynier et al. (2012) (Tokyo Tech)	0.056492	0.000002	Static	<del>53</del> 53
Andreasen and Sharma (2007)	0.056494	0.000002	Static	<del>577</del> 12

\*Both studies used the same Triton TIMS instrument at ETH Zürich.

**Table 4**The  $\epsilon^{84}\text{Sr}$  values for BCR-2, BHVO-2, and BSE acquired in static (line 1) and dynamic modes.

	Static $\epsilon^{84}\text{Sr}$	2SD	2SE	n
<b>SRM 987 (column processed, this study)</b>	-0.06	0.39	0.17	<del>580</del> 5
<b>BCR-2</b>				581
This study	-0.20	0.46	0.15	10
Hans et al. (2013b)	-0.32	0.26	0.11	<del>582</del> 3
Brennecke et al. (2013)	-0.10	0.50	0.25	4
Andreasen and Sharma (2007)	-0.16	0.45	0.17	<del>583</del> 3
Paton et al. (2013)	-0.18	0.30	0.10	10
<b>BHVO-2</b>				584
This study	-0.13	0.35	0.14	6
Hans et al. (2013b)	-0.16	0.30	0.17	<del>585</del> 3
Yobregat et al. (2017)	-0.07	0.31	0.10	9
Moynier et al. (2012)	-0.18	0.31	0.22	<del>586</del> 6
Paton et al. (2013)	-0.25	0.22	0.06	16
<b>BSE</b>				587
This study	-0.15	0.45	0.09	27
Hans et al. (2013b)	-0.25	0.26	0.07	<del>588</del> 4
Yobregat et al. (2017)	-0.14	0.41	0.10	17
Moynier et al. (2012) (TT)	-0.29	0.20	0.08	<del>589</del> 9
Paton et al. (2013)	-0.22	0.26	0.05	26
	<b>Dynamic <math>\epsilon^{84}\text{Sr}</math></b>	<b>2SD</b>	<b>2SE</b>	<b>590</b>
<b>SRM 987 (column processed, this study)</b>	-0.08	0.43	0.19	5
<b>BCR-2</b>				591
This study	-0.12	0.36	0.11	10
Hans et al. (2013a)	0.04	0.09	0.04	5
<b>BHVO-2</b>				592
This study	0.04	0.60	0.24	6
Hans et al. (2013a)	0.04	0.31	0.18	<del>593</del> 3
Yobregat et al. (2017)	-0.07	0.31	0.10	9
<b>BSE</b>				594
This study	-0.04	0.49	0.09	28
Hans et al. (2013a)	0.02	0.24	0.07	<del>595</del> 14
Yobregat et al. (2017)	-0.03	0.29	0.07	17
				<del>596</del>



597

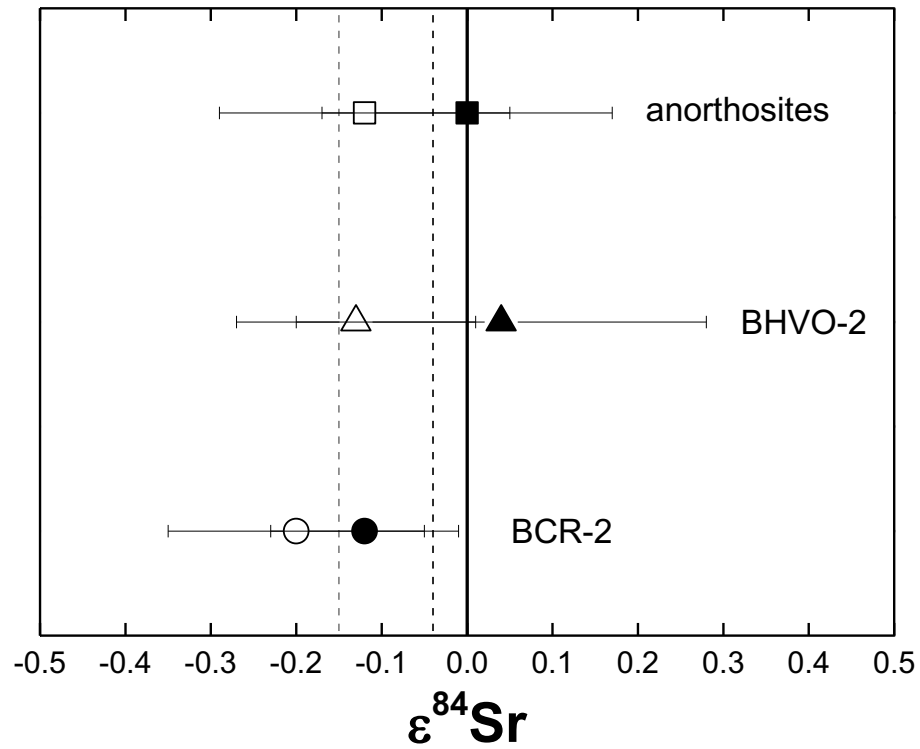
598 **Fig. 1.** Strontium isotopic data for terrestrial samples acquired in dynamic and static (line  
 599 1) modes. The  $\epsilon^{84}\text{Sr}$  values were calculated relative to the NIST SRM 987 Sr isotopic  
 600 standard. The grey lines are  $\pm 49$  ppm (dynamic) and  $\pm 45$  ppm (static) (2SD for all rocks).  
 601 The dashed lines represent the average  $\epsilon^{84}\text{Sr}$  values of all rocks:  $-0.04$  (dynamic) and  $-$   
 602  $0.15$  (static).  
 603

604

605

606

607



608

609 **Fig. 2.** Mean  $\epsilon^{84}\text{Sr}$  values for BCR-2 (n=10), BHVO-2 (n=6), and all anorthosites (AN-G,  
 610 JL-27, AN-1, AN-2; n=10) for dynamic (filled symbols) and static line 1 (open symbols)  
 611 data acquisition modes. Error bars are 2SE. The black dashed line (dynamic) and gray  
 612 dashed line (static) are the averages of all terrestrial samples analyzed (n=27).  
 613

614

615

616

617

618

619

620

621

622